Network Model of Flow, Transport and Biofilm Effects in Porous Media

Brian J. Suchomel, Institute for Mathematics and its Applications
University of Minnesota, Minneapolis, Minnesota 55455.

Benito M. Chen, Department of Mathematics
University of Wyoming, Laramie, Wyoming 82071.

Myron B. Allen III, Department of Mathematics
University of Wyoming, Laramie, Wyoming 82071.

August 27, 1997

Abstract

In this paper we develop a network model to determine porosity and permeability changes in a porous medium as a result of changes in the amount of biomass. The biomass is in the form of biofilms. Biofilms form when certain types of bacteria reproduce, bond to surfaces, and produce extracellular polymer (EPS) filaments that link together the bacteria. The pore spaces are modeled as a system of interconnected pipes in two and three dimensions. The radii of the pipes are given by a lognormal probability distribution. Volumetric flow rates through each of the pipes, and through the medium, are determined by solving a linear system of equations, with a symmetric and positive definite matrix. Transport through the medium is modeled by upwind, explicit finite difference approximations in the individual pipes. Methods for handling the boundary conditions between pipes and for visualizing the results of numerical simulations are developed. Increases in biomass, as a result of transport and reaction, decrease the pipe radii, which decreases the permeability of the medium. Relationships between biomass accumulation and permeability and porosity reduction are presented.

KEYWORDS: biofilm, network model, porous media, permeability

1 Introduction

Biofilms — complexes of bacterial biomass and extracellular polymer — have a variety of interesting effects when they grow in porous media. Typically, the presence of biofilms in the voids of a porous medium reduces its permeability and porosity. This fact suggests a wide range of applications in the control of groundwater contaminant transport and production from oil reservoirs. This paper presents a network model of fluid flow and the transport and growth of biofilms in a porous medium.

There is a fundamental difficulty in modeling the effects of biofilm growth and transport in porous media: The microscopic dynamics, best understood at the scale of individual pores, affect macroscopic flow properties such as permeability and porosity, which are meaningful at much coarser scales. This is the *scale-up* problem. The purpose of our model is to help scale up from a simplified but reasonable representation of the microscopic physics to the scale described by macroscopic flow properties. The macroscale we wish to model is on the order of a soil column in a lab, where the soil is spatially homogeneous, but where there are variations in pore sizes at the microscale.

Several researchers have studied biofilms and their effects on porous media. Vandeviver and Baveye (1992) experimentally investigate a relationship between transport and clogging for biofilms. Other researchers, including Tan et al. (1994) and Lindqvist et al. (1994), develop models of porous media based on the continuum hypothesis, including transport and sorption of bacteria, and use physical experiments to test their models. Taylor and Jaffé (1990a,b,c) show experimentally that permeability reductions up to a factor of 5×10^{-4} can be obtained and investigate the relationship between biomass and permeability reduction. They also investigate a biofilm's effect on dispersivity.

There also exists a large literature on network models of porous media. Among the applications most pertinent to our work are those that investigate particle entrapment (Rege and Fogler, 1986) and (Sahimi and Imdakm, 1991). Koplik (1982) compares flow properties derived from network models to that predicted by effective-medium theory. Koplik and Lasseter (1982) investigate immiscible displacement on a two-dimensional network model. Simon and Kelsey (1971, 1972) model miscible displacement on a network model. Sugita, Gillham and Mase (1995) use particle tracking to model solute transport on a network model.

In this paper we construct a network flow model and show that the resulting system of equations may be solved using an iterative SOR technique. We develop a new method for modeling transport on a network model and consider some of the method's numerical properties such as stability and numerical diffusion. We describe how the growth of a biofilm may be incorporated into the model and how to account for resulting changes in the permeability and porosity of a porous medium. We present numerical results showing that the network obeys Darcy's law macroscopically. We also show that our method of modeling transport behaves similarly to, but not exactly the same as, classical continuum solutions to the advection-diffusion equation. Finally, we include results of some numerical simulations of flow and transport of nutrients accompanied by biofilm growth.

A sequel to this paper (Suchomel et al.) describes scale-up results in more detail.

There are two main contributions of this paper. The first is a proof that a network model yields a symmetric, positive-definite linear system. This is curiously lacking from the literature. The second is a new method for modeling transport in a network model. This numerical method makes it easy to add terms that model other physical phenomena and couple equations representing a number of solutes. These physical phenomena may include, but are not limited to, reaction kinetics, adsorption, and erosion. The extra terms may be linear or non-linear.

2 Development of the Flow Model

Scientists have used network models to describe flow through porous media for over 40 years. One of the earliest examples is the work of Fatt (1956). The idea is to avoid detailed geometric description of the pore spaces — which is essentially impossible in natural porous media (Scheidegger, 1957) — in favor of idealized descriptions that preserve macroscopic properties of the media. In our setting, network models can help quantify how bacterial transport and biofilm growth affect permeability and porosity. In this section we develop a model of porous media based on networks of pipes and junctions. We derive a system of equations that describes flow through this network and examine properties of this system that are relevant to its numerical solution.

Network geometry

We represent the pore spaces by a network of interconnected, cylindrical pipes with random radii, assigned according to a lognormal probability distribution. We refer to the physics of individual pipes and the junctions that connect them as the *microscale*. We use lower case letters to denote microscale quantities. For example, the pressure head at junction i is h_i; the flow through the pipe connecting junctions i and j is $q_{i,j}$. (Sometimes it is useful to index pipes according to the junctions that they connect; sometimes it is more useful to index pipes with a single subscript.) Our goal is to understand the *macroscale*, that is, the overall physics of the network, in terms of statistical properties of the microscale. We use upper-case letters to denote macroscale quantities. For instance, Q is the total flow rate through the network.

The issue arises whether the network's topology should be random or regular, in the sense that all interior junctions have the same number of intersecting pipes. Since regular grids are much easier to work with computationally, we use them in this study. By examining Voronoi tesselations as archetypical random networks, Jerauld et al. (1983a,b) argue that properties derived from the analysis of regular networks are virtually the same as those derived from networks with random topologies.

Many possible regular configurations exist. Figure 1 shows rectangular and hexagonal networks in two space dimensions. In three dimensions we use cubic networks. The *coordination number* of a regular network is the number of pipes that intersect at an interior junction. Thus a rectangular network has coordination number 4; a cubic network has coordination number 6.

There also arises the issue whether pipe lengths should be random or constant. It is possible to assign pipe lengths according to some probability distribution, to account for tortuosity. However, the choice between fixed and random pipe lengths seems to make little difference in the macroscale

flow properties of a network (van Brakel, 1975). On the strength of this observation, we assume that all pipes have the same length, ℓ.

We designate left-to-right as the overall (horizontal) flow direction, determined by the macroscopic head gradient. Denote by M the number of junctions in the flow direction; let N be the number of junctions in the vertical direction, and in three dimensions let P be the number of junctions in horizontal direction orthogonal to the overall flow direction. Thus the size of a two-dimensional rectangular grid is $M \times N$, and the size of a three-dimensional cubic grid is $M \times N \times P$.

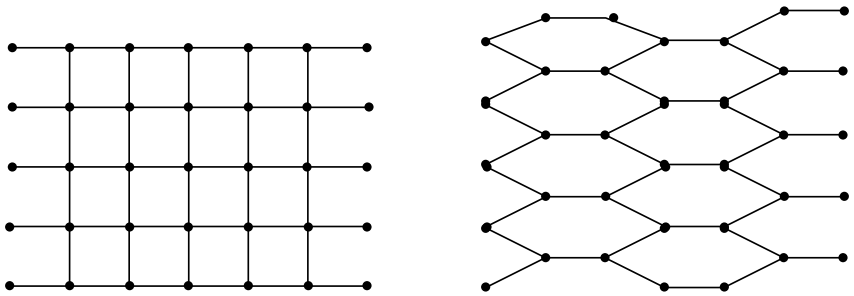

Figure 1: Square and hexagonal networks used to model two-dimensional porous media. Both networks have size 7×5.

Flow physics

We specify the flow physics at the microscale, using these physics to compute quantities needed to characterize the flow at the macroscale. At the microscale, all flow occurs through the interconnected pipes, and no fluid accumulates at the junctions. In an individual pipe having radius $a_{i,j}$, the flow rate $q_{i,j}$ obeys the Hagen-Poiseuille equation,

$$q_{i,j} = \hat{k}_{j,i}\,(h_i - h_j)\,, \tag{1}$$

where $q_{i,j}$ is the flow into junction j from junction i through the pipe, h_j and h_i are the values of head at junctions j and i, respectively, and $\hat{k}_{j,i} = \rho g \pi a_{i,j}^4/(8\mu L)$. Here ρ is the density of the fluid, g is the acceleration of gravity, and μ is the viscosity of the fluid.

Mass balance implies that, at each junction j,

$$\sum_{i=1}^{N_{p,j}} q_{i,j} = \sum_{i=1}^{N_{p,j}} \hat{k}_{j,i}\,(h_i - h_j) = 0, \qquad \text{for all junctions } j.$$

Here $N_{p,j}$ is the number of pipes connected to junction j. Thus the flow equation is a linear system of the form $\mathbf{A}\vec{h} = \vec{b}$, where $\vec{h}$ is a vector of unknown head values at the interior junctions. The prescribed head values at the junctions on the inlet and outlet sides of the network appear in the vector $\vec{b}$.

The macroscale volumetric flow rate Q through the grid is the sum of the microscale flow rates through the outlet side of the grid. Under the hypothesis that the macroscale flow obeys Darcy's law, the permeability of the network is

$$K = -\frac{QL}{A\,\Delta H},$$

where A is the cross-sectional area of the network, L is its length, and ΔH is the net head drop between its left and right boundaries. We discuss the Darcy hypothesis in section 7.

Solving the linear system

We now show that the coefficient matrix, $\mathbf{A}$, for the flow equation is sparse, symmetric, weakly diagonally dominant, irreducible, and positive definite.

First, consider the zero structure of $\mathbf{A}$. In two dimensions, a square grid has a coordination number of 4, while a hexagonal grid has a coordination number of 3. In three dimensions, a cubic grid has a coordination number of 6. Therefore, the matrix $\mathbf{A}$ for a square grid has at most four nonzero off-diagonal elements in a row. The matrix for a hexagonal grid has at most three nonzero off-diagonal elements in a row, and a cubic grid has at most six. Similarly, $\mathbf{A}$ has at most four, three, and six off-diagonal entries, respectively, in each column.

Next, we establish that $\mathbf{A}$ is symmetric. The mass balance furnishes one equation for each node. Alternatively, we may view each pipe as directly influencing two equations. In a two-dimensional square grid, consider the pipe connecting junctions α and β, with flow coefficient $\hat{k}_{\alpha,\beta}$, as shown in figure 2. Associated with junction α is a row in $\mathbf{A}$ representing the equation

$$\hat{k}_{a1,\alpha}\left(h_\alpha - h_{a1}\right) + \hat{k}_{a2,\alpha}\left(h_\alpha - h_{a2}\right) + \hat{k}_{a3,\alpha}\left(h_\alpha - h_{a3}\right) + \hat{k}_{\alpha,\beta}\left(h_\alpha - h_\beta\right) = 0.$$

We can rearrange this equation as follows:

$$\left(\hat{k}_{a2,\alpha} + \hat{k}_{\alpha,\beta} + \hat{k}_{a1,\alpha} + \hat{k}_{a3,\alpha}\right) h_\alpha - \hat{k}_{\alpha,\beta} h_\beta - \hat{k}_{a1,\alpha} h_{a1} - \hat{k}_{a2,\alpha} h_{a2} - \hat{k}_{a1,\alpha} h_{a1} = 0. \tag{2}$$

Therefore the diagonal entries are positive. Also the entry $a_{\alpha,\beta}$ in the matrix $\mathbf{A}$ is $-\hat{k}_{\alpha,\beta}$. Associated with junction β we have the equation

$$\left(\hat{k}_{\alpha,\beta} + \hat{k}_{b1,\beta} + \hat{k}_{b2,\beta} + \hat{k}_{b3,\beta}\right) h_\beta - \hat{k}_{\alpha,\beta} h_\alpha - \hat{k}_{b1,\beta} h_{b1} - \hat{k}_{b2,\beta} h_{b2} - \hat{k}_{b1,\beta} h_{b1} = 0. \tag{3}$$

Thus $a_{\beta,\alpha} = -\hat{k}_{\alpha,\beta} = a_{\alpha,\beta}$ when α and β are indices of adjacent junctions. For nonadjacent junctions α and β, $a_{\alpha,\beta} = 0 = a_{\beta,\alpha}$. It follows that the matrix $\mathbf{A}$ is real and symmetric, and, therefore, all eigenvalues of $\mathbf{A}$ are real. Similar reasoning applies to hexagonal and cubic networks.

Equation (2) shows that $\mathbf{A}$ is weakly diagonally dominant:

$$|a_{ii}| \geq \sum_{j=1, j\neq i}^{n} |a_{ij}|\,. \tag{4}$$

Moreover, for rows corresponding to junctions on the boundary of the grid where the pressure head is set to 0,

$$|a_{ii}| > \sum_{j=1, j\neq i}^{n} |a_{ij}|\,. \tag{5}$$

By Gershgorin's Theorem (Kincaid and Cheney, 1991, p.240), all eigenvalues of $\mathbf{A}$ lie in disks located to the right of the imaginary axis, with possibly some but not all of the disks touching the imaginary axis. Therefore all of the eigenvalues are greater than or equal to zero. The matrix is irreducible because of the physical system from which it is constructed. The grid is connected.

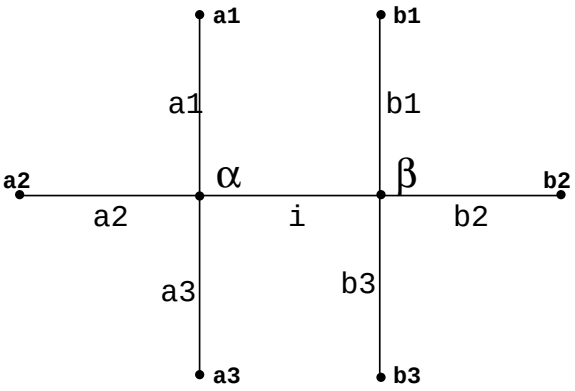

Figure 2: Subset of a rectangular network. Junctions are labeled in boldface, and pipes are labeled in larger letters.

Zero is a boundary point of the union of the closed disks, but it is not an eigenvalue of $\mathbf{A}$, since it is not a boundary point of each of the closed disks (Brualdi and Ryser, 1991, §3.6). Hence, the matrix $\mathbf{A}$ is positive definite.

The symmetry and positive definiteness of $\mathbf{A}$ guarantee that the successive overrelaxation (SOR) method converges for the linear system $\mathbf{A}\vec{h} = \vec{b}$ for values of the relaxation parameter between 0 and 2 (Young, 1971, Chapter 4). Such an iterative scheme has important advantages for our model, beyond the usual advantages associated with minimizing storage. When we include bacterial transport and growth in the model, the radii of the pipes change as biofilm accumulates. In this case, the flow properties of the network change, and we must solve the flow equation repeatedly during a single simulation. By using SOR, we may take the most recent values of head as initial guesses for the succeeding time step, thereby speeding convergence.

We use a residual criteria for convergence. Define the vector $\vec{r}$ by

$$r_i = b_i - \sum_{j=1}^{n} a_{i,j} h_j \,.$$

We iterate until $\max\{r_i\} \leq \epsilon$, where ϵ is some pre-set tolerance. We compute $\vec{r}$ every tenth iteration. The residual at node i amounts to the sum of volumetric flow rates out of that node.

3 Development of the Transport Model

Modeling biofilm growth in the network requires solving for the transport of biofilm-forming bacteria through the pipes. Among the earliest work in modeling transport in networks is that of Simon and Kelsey (1971). They model miscible displacement of one fluid by another by tracking concentration fronts in the pipes, assuming complete mixing at the junctions. Sugita, Gillham and Mase (1995) use a particle-tracking technique, in which each computational particle represents a given mass of solute.

In contrast, we adopt an Eulerian viewpoint and model concentrations at fixed points in the network. More specifically, we use finite differences to model transport in each of the individual pipes. In this section we describe this transport model in detail.

Transport physics

We model transport within each pipe p as a one-dimensional process obeying the equation

$$\frac{\partial u}{\partial t} + \bar{v}_p \frac{\partial u}{\partial x} - D \frac{\partial^2 u}{\partial x^2} = 0. \tag{6}$$

Here, D is the longitudinal (axial) diffusion coefficient, u is concentration, and $\bar{v}_p$ is the mean velocity through the pipe.

We calculate $\bar{v}_p$, using the microscopic flow equation, as follows: The heads at the junctions of the network determine the volumetric flow rates through individual pipes via equation (1). We compute the mean fluid velocity through pipe p by dividing the volumetric flow rate by the cross-sectional area of the pipe,

$$\bar{v}_p = \frac{q_p}{\pi a_p^2}. \tag{7}$$

We discuss the treatment of longitudinal diffusion, D, shortly.

Discretizing the pipes

The grid used to model transport is a refinement of the pipe-junction network used to solve the flow equations, in the sense that the transport grid discretizes individual pipes. Figure 3 shows the relationship between the flow network and the transport grid. The solid dots represent junctions of the network. The open circles signify nodes in the grid used for solving transport. This transport grid divides each pipe into uniform cells. Different pipes may be partitioned differently, according to criteria discussed below. If the cells in a given pipe p have length Δx_p, their volume is $\pi a_p^2 \Delta x_p$. There is no volume associated with the nodes of the transport grid.

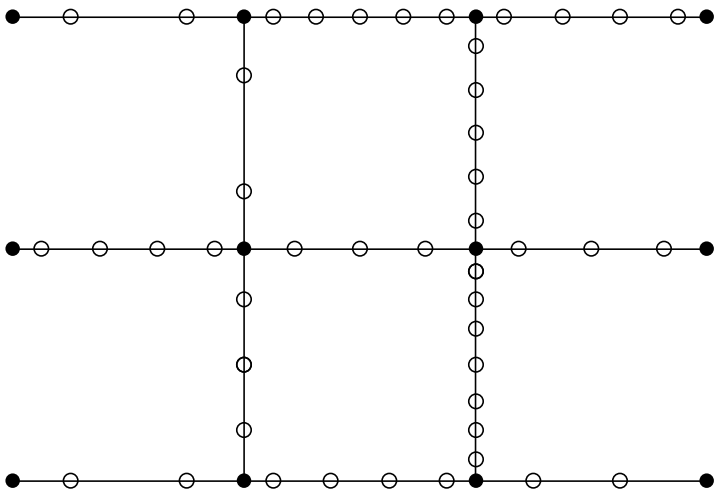

Figure 3: Discretizations used for solving flow and transport equations. The solid dots are junctions of the network on which we solve the flow equation. The open dots are nodes of the grid used for transport calculations.

The transport grid serves as a vehicle for discretizing equation (6). In each pipe, we use an

upwind, explicit finite-difference approximation,

$$\frac{\left(u_i^{n+1} - u_i^n\right)}{\Delta t} + \bar{v}_p \frac{\left(u_i^n - u_{i-1}^n\right)}{\Delta x_p} = 0, \tag{8}$$

or

$$u_i^{n+1} = \lambda_p \; u_{i-1}^n + (1 - \lambda_p)\, u_i^n, \tag{9}$$

where

$$\lambda_p = \frac{\bar{v}_p \Delta t}{\Delta x_p}. \tag{10}$$

The scheme is stable whenever $\lambda_p \leq 1$.

In this approximation, we assume that $D = 0$, even though both advection and diffusion occur physically. Our reasoning is as follows: An upwind, explicit scheme inherently contains numerical diffusion. By partitioning the pipes appropriately, we can adjust the numerical diffusion to control the effective diffusion in the pipes. We now discuss the details of this procedure.

Controlling numerical diffusion

To quantify the numerical diffusion in equation 8, we examine Taylor expansions for each term about a point midway between spatial nodes $i-1$ and i and midway between time levels n and $n+1$. Substituting these expansions into the scheme yields

$$\begin{aligned}\frac{\left(u_i^{n+1} - u_i^n\right)}{\Delta t} + \bar{v}_p \frac{\left(u_i^n - u_{i-1}^n\right)}{\Delta x_p} \quad &= \quad \left.\frac{\partial u}{\partial t}\right|_{i-\frac{1}{2}}^{n+\frac{1}{2}} + \bar{v}_p \left.\frac{\partial u}{\partial x}\right|_{i-\frac{1}{2}}^{n+\frac{1}{2}} + \frac{(\Delta x_p - \bar{v}_p \Delta t)}{2} \left.\frac{\partial^2 u}{\partial x \partial t}\right|_{i-\frac{1}{2}}^{n+\frac{1}{2}} \\ &\quad + \mathcal{O}((\Delta x_p + \Delta t)^2).\end{aligned}$$

The first two terms on the right are identical to those in the diffusion-free transport equation. By using the transport equation, we write the mixed derivative in the third term on the right as

$$-D_p^{num} \left.\frac{\partial^2 u}{\partial x^2}\right|_{i-\frac{1}{2}}^{n+\frac{1}{2}},$$

where

$$D_p^{num} = \frac{\bar{v}_p \Delta x_p \,(1 - \lambda_p)}{2}. \tag{11}$$

Thus, up to $\mathcal{O}((\Delta x_p + \Delta t)^2)$, the scheme (8) approximates the diffusion-free transport equation and adds numerical diffusion given by equation (11).

This analysis allows us to control the numerical diffusion generated in the individual pipes by adjusting the numbers $N_1, N_2, \ldots, N_P$ of cells in each of the pipes, indexed $1, 2, \ldots, P$, and the common time step Δt. To facilitate the discussion, we define dimensionless position and time variables

$$\xi = \frac{x}{L}, \qquad \tau_p = \frac{\bar{v}_p t}{L}.$$

In terms of these variables, the cell length in pipe p is $\Delta\xi_p = 1/N_p$, and the numerical diffusion there is

$$D_p^{num} = \frac{\bar{v}_p L\left(\Delta\xi_p - \Delta\tau_p\right)}{2} \tag{12}$$

$$= \frac{\bar{v}_p L}{2}\left(\frac{1}{N_p} - \Delta\tau_p\right). \tag{13}$$

Stability requires that $D_p^{num} \geq 0$, which implies that

$$\Delta t \leq \frac{L}{\bar{v}_p N_p}, \qquad k = 1, 2, \ldots, P. \tag{14}$$

To impose this condition across the entire network, we choose

$$\Delta t \leq \frac{L}{|\bar{v}_{max}|\, N_{min}}, \tag{15}$$

where N_{min} is the smallest number of cells allowed in any pipe and $\bar{v}_{max}$ is the largest-magnitude mean velocity occurring among the pipes. This way, if we assign $N_p = N_{min}$ for any pipe in which $|\bar{v}_p| = |\bar{v}_{max}|$, we have $D_k^{num} = 0$ in that pipe. To minimize numerical diffusion elsewhere, we divide other pipes into as many cells as possible, subject to the constraint that

$$N_p \leq \frac{L}{\bar{v}_p \Delta t}.$$

In other words, we want

$$N_p \leq \frac{1}{\Delta\tau_p} \leq N_p + 1. \tag{16}$$

When the flow through a pipe is very slow, the criterion (16) calls for very large values of N_p. To avoid impractical computational expense, we set an upper bound N_{max} on the number of cells allowed in any pipe. Thus,

$$N_p = \min\left\{\left\lfloor \frac{1}{\bar{v}_p \Delta t}\right\rfloor, N_{max}\right\}, \tag{17}$$

where $\lfloor\cdot\rfloor$ denotes the greatest integer function.

If we choose N_{max} to be the smallest positive integer satisfying

$$N_{max} \geq \frac{\sqrt{N_{min}\left(N_{min}+1\right)^2}}{2}, \tag{18}$$

then the numerical diffusion generated in any pipe obeys the bound

$$\max\left(D_p^{num}\right) \leq \frac{\bar{v}_{max} L}{2\left(N_{min}+1\right)^2}. \tag{19}$$

4 Boundary Conditions

In this section we present a method for handling boundary conditions at the ends of the pipes. Consider junction α in figure 4. Four different equations contain the concentration at junction α in our finite-difference approximation to the transport equation. The fluid velocities and cell

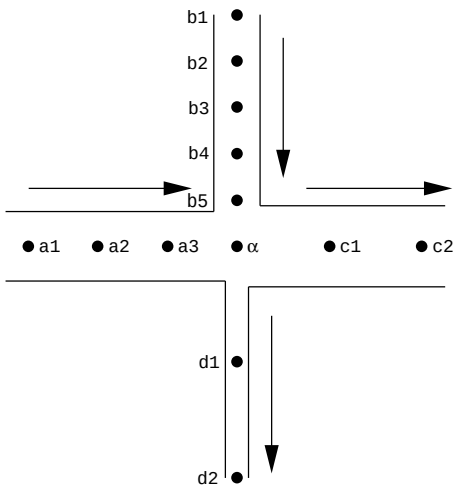

Figure 4: The pipes surrounding node α. Flow directions in the pipes are indicated by the arrows.

volumes in the surrounding pipes may be different. Because of this fact, some care is required in the treatment of boundary conditions for the transport calculations.

Naively, we might seek a single value for concentration at junction α, which would serve as a common boundary value for all of the pipes adjacent to the junction. However, a simple example illustrates why this is impossible. In our finite-difference scheme, the concentration at junction α would have to obey both of the following equations:

$$u_\alpha^{n+1} = \lambda_a u_{a3}^n + (1-\lambda_a) u_\alpha^n,$$

and

$$u_\alpha^{n+1} = \lambda_b u_{b5}^n + (1-\lambda_b) u_\alpha^n,$$

where $\lambda_a = \bar{v}_a \Delta t / \Delta x_a$ and $\lambda_b = \bar{v}_b \Delta t / \Delta x_b$. These equations need not give the same value for u_α.

We overcome this difficulty by using an averaging scheme to determine the concentrations at pipe inlets and outlets. If we assume that the fluid undergoes plug flow, then equation (9) is a mixing rule: During one time step, a fraction λ of the volume of cell i is replaced by fluid of concentration u_{i-1}^n from cell $i-1$. Figure 5 illustrates this interpretation. Thus $(1-\lambda)$ is the fraction of the cell's volume that remains occupied by fluid with concentration u_i^n. The linear combination $\lambda u_{i-1}^n + (1-\lambda)\, u_i^n$ gives the new concentration of cell i.

Suppose that cell i is adjacent to the inlet of a pipe. The mixing analogy suggests that the new concentration of cell i depends on the old concentration of cell i itself and the concentrations flowing into the inlet. Since there may be one or more pipes contributing to flow into this inlet junction, the net concentration $u_{A,i-1}^n$ flowing into cell i is a linear combination of the concentrations in cells from other pipes adjacent to the inlet junction, as illustrated in figure 6. The appropriate linear combination is a flow-weighted average: If u_j^n, $j = 1, 2, \ldots, J$, are the concentrations in the

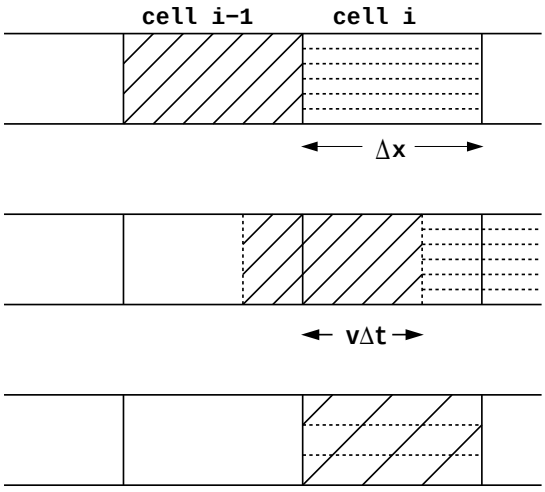

Figure 5: Interpretation of λ as the fraction of the cell that the fluid moves through in one time step Δt.

cells just upstream of the inlet, then

$$u^n_{A,i-1} = \frac{\sum_{j=1}^{J} u^n_j q_j}{\sum_{j=1}^{J} q_j} \tag{20}$$

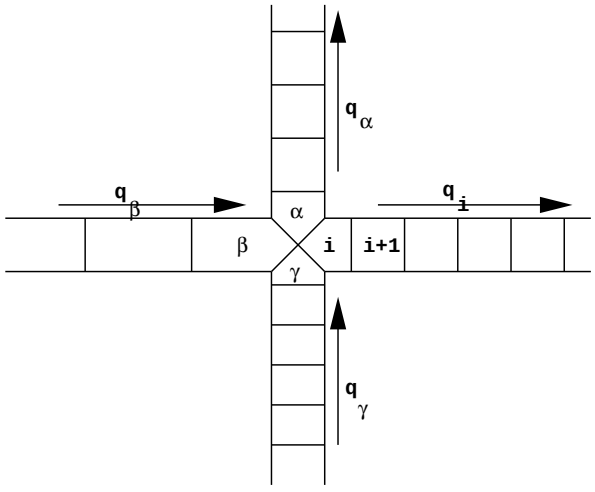

Figure 6: The cells surrounding a junction. Cell i is at the inlet side of a pipe. Flow directions in the pipes are indicated by the arrows. All cell radii appear equal; in general they are different.

This treatment of the boundary conditions for transport requires us to distinguish between flows into and out of a given junction. In coding such a scheme, one must store the indices of the pipes that meet at a each junction, along with the direction of the flow from each pipe.

Other authors have proposed models for partial mixing at junctions. Hull and Koslow (1986) investigate streamline routing in 2-D planar, perpendicular junctions. Philip (1988) does a more thorough investigation of the same phenomena. Both sets of authors assume perpendicular junctions with very simple geometries. Naturally occuring porous media do not exhibit these characteristics. We have neglected tortuosity factors in our pipe lengths and volume at the junctions in our model. We do not presume that pipes enter junctions at right angles. We use a simple flow weighted average, which assumes complete mixing, as a reasonable approximation. Our model does allow for there to be either only one pipe entering or one pipe leaving a junction, in which case, either no mixing is encountered, or complete mixing is the only possibility.

5 Visualization

In any computational study of scale-up from microscale to macroscale, the issue of visualization arises. In our model, flow and transport are essentially one-dimensional at the microscopic scale, but they may be two- or three-dimensional macroscopically, depending on the type of network used. Displaying all of the pipe radii and flow rates and the concentrations in all cells at each time level requires animation of a finely detailed database.

Instead, we adopt a simpler visualization scheme that still captures the macroscopic behavior of the system. We display mean concentrations at the junctions of the network, calculated in a fashion similar to that used to calculate inlet concentrations in the transport model. However, for visualization, we use weighted averages based on static volumes (or, equivalently, cross sectional areas) of the pipes meeting at a junction, rather than on flow rates. To illustrate this scheme, consider the junction shown in figure 6. Let a_α, a_β, a_γ, and a_i be the radii of the pipes surrounding the node and let c_α, c_β, c_γ, and c_i be the corresponding concentrations at the midpoints of the cells bordering the node. The static-volume averaging scheme yields the following concentration at the node:

$$c_{node} = \frac{c_\alpha a_\alpha^2 + c_\beta a_\beta^2 + c_\gamma a_\gamma^2 + c_i a_i^2}{a_\alpha^2 + a_\beta^2 + a_\gamma^2 + a_i^2}.$$

To plot solute concentration as a function of depth in a square network, we calculate the average concentration over all junctions in each column. Again, we use static-volume averaging: In column j, the average concentration is

$$c_j = \frac{\sum_{i=1}^{N} \left(\sum_\alpha c_{i,j,\alpha} a_{i,j,\alpha}^2 \right)}{\sum_{i=1}^{N} \left(\sum_\alpha a_{i,j,\alpha}^2 \right)}.$$

In this equation, i indexes the row in the network, j indexes the column, and the triple (i, j, α) indexes the α^{th} cell bordering on the junction at row i, column j. This cell has radius $a_{i,j,\alpha}$.

In three-dimensional networks, we display breakthrough curves by averaging the concentrations of cells at the outlet side of the network, using flow rates for the weighting. If α, β, ... are the indices of the cells adjacent to the outlet side of the network, with corresponding volumetric flow

rates q_α, $q_\beta, \ldots$, the macroscopic effluent concentration is

$$C_{out} = \frac{c_\alpha q_\alpha + c_\beta q_\beta + \cdots}{q_\alpha + q_\beta + \cdots}.$$

6 Inclusion of Biofilm Phenomena

Modeling biofilm growth and transport in the network requires keeping track of at least two species: bacteria and nutrients. We also assume that we have two phases present within the pipes: a solution phase and an adsorbed (biofilm) phase. The total volume of a pipe is fixed at the beginning of a simulation. It is divided evenly among the cells in the pipe. The solution phase occupies the entire volume of a cell. The adsorbed phase occupies a portion of the volume of a cell determined by its concentration and density. Physically, a biofilm is composed mainly of fluid (Christensen and Characklis, 1990). We consider it, not as a solid, but as a phase occupying a certain volume which may also be occupied by species in the solution phase. We ignore transport processes between the bulk phase and the biofilm. The biofilm decreases the effective radius of a cell. This decreases the effective conductivity of the cell, and hence the conductivity of the pipe.

We treat each cell in the transport grid as a tank reactor connected only to cells that are immediately upstream or downstream. Within each cell, species concentrations are spatially uniform, and some of a species' mass may be in the adsorbed phase (biofilm), while the rest is in solution. Mass in solution undergoes transport via advection, while adsorbed mass undergoes no advection or diffusion. The concentrations of the species are coupled, since bacteria consume nutrients. In addition, there may be some mass transport of bacteria between phases.

We incorporate adsorption into our model with a novel approach. The thickness of the biofilm influences the radius of a pipe. Let a_o be the radius initially assigned to a pipe by the probability distribution. We assume that any concentration of a species in the adsorbed phase adheres to the walls of the pipe, decreasing its effective radius by an amount equal to the thickness of the biofilm. The dissolved species do not affect the size of a pipe. Let c_B be the total adsorbed concentration in a cell, and let ρ_B be the density of the biofilm. The fraction c_B/ρ_B has units of biofilm volume per cell volume. The radius at time t is

$$a_t = a_o \sqrt{1 - \frac{c_B(t)}{\rho_B(t)}}. \tag{21}$$

The biofilm thickness in the cell is therefore

$$d_{B,t} = a_o - a_t.$$

Mass is conserved in all components at each step. In solving the flow equation we impose a no accumulation condition at each node. We have conservation of mass between species within each cell. All carbon lost from the nutrient concentration is accounted for as gains in other concentrations. Mass transfer of bacteria between the adsorbed and solution phases does not affect total mass. Since we assume that the solution phase occupies the entire cell, there is no loss of fluid.

A biofilm affects the radii of the pipes, which in turn affect the coefficients $\hat{k}$ in the flow equation. In principle, biofilm-induced changes in pipe radii require us to solve the flow equations

iteratively at each time level, to account for the coupling between flow and transport. When biofilm growth is slow enough, the flow properties of the network do not change significantly within a time step, and computationally it may not be necessary to solve the flow equation at every time step. Instead, to reduce computational expense, we assume that the pipe velocities remain unchanged for several time levels.

When we do compute new flow rates through the grid, we redistribute biofilm concentrations. We calculate the biofilm concentration of a pipe as the arithmetic mean of the concentrations of the individual cells in the pipe. Then we calculate the new radii of the pipes using equation (21) and use these radii to calculate $\hat{k}$ values.

At the beginning of a simulation all of the pipes have positive radii. As a simulation progresses and a biofilm grows in the pipes, some of the radii may go to zero. The matrix becomes singular if all of the pipes meeting at any given node become zero at the same time. This corresponds to a zero row in the matrix and a zero right hand side. Any value for pressure head is acceptable at that node since there will not be any flow into or out of the node for any h. We essentially decrease the number of unknowns by one when this happens. Another situation can develop which causes more significant numerical problems. There will be no solution to $\mathbf{A}\vec{h} = \vec{b}$ when a whole column of connected nodes have zero flow, and our iterative scheme will not converge. This corresponds physically to complete clogging of the medium. Simulation results no longer make sense after this point.

A complete description of the PDEs and ODEs used in incorporating biofilm effects into a network model may be found in a subsequent paper (Suchomel et al.). We also describe reaction and phase change kinetics along with stability criteria and a stable integration scheme.

7 Numerical Results

To verify that the coupled flow-and-transport model produces physically reasonable results, we examine numerical results from several model problems. We assess whether the flow model produces macroscopic velocities consistent with Darcy's law, whether the transport model yields macroscopic plumes that agree with standard models of hydrodynamic dispersion, and whether the coupled model computes plausible results for biofilm growth and transport. In a subsequent paper (Suchomel et al.) we present more detailed results relating to the scale-up of biofilm growth and transport.

We begin with the flow calculations. Here the question is whether it is reasonable to calculate a macroscopic permeability by averaging the results of the microscopic model. Many naturally occurring porous media have irregular pore spaces with some degree of randomness in their configurations. We expect some small variations in the permeabilities in different samples of these substances. By analogy, within any suite of networks having pipe radii assigned from a fixed probability distribution, we expect some variations in the apparent macroscale permeability.

Figure 7 shows how the ratio $Q/\Delta H$ varies within suites of 100 20×20 networks, each suite having pipe radii assigned from a lognormal distribution having mean $\mu = 1$. The figure shows histograms of $Q/\Delta H$ for four different choices of standard deviation in the lognormal distribution. We conclude from this figure that apparent macroscale permeabilities tend to cluster around a

central, representative value, especially at smaller values of standard deviation. This result is expected since smaller standard deviations represent more homogeneous media. We use $\sigma = .6$ for most of our calculations since it represents an average porous medium. Values used by other authors range from $\sigma = .02$ to $\sigma = 1.2$. Sugita et al. (1995) claim that $\sigma = 0.2$ to 0.3 is representative of an actual homogeneous porous medium and Imdakm and Sahimi (1991) claim that $\sigma = \frac{2}{3}$ closely approximates experimentally-determined pore size distributions of Ottawa sandpack.

Of more direct interest is the question whether $Q/\Delta H$ varies linearly with the length of the medium—that is, whether Darcy's law is a valid hypothesis for the macroscopic flow. Figure 8 suggests that the Darcy's hypothesis is valid and that, for a given length, the medium's permeability decreases as the standard deviation in pipe diameters increases.

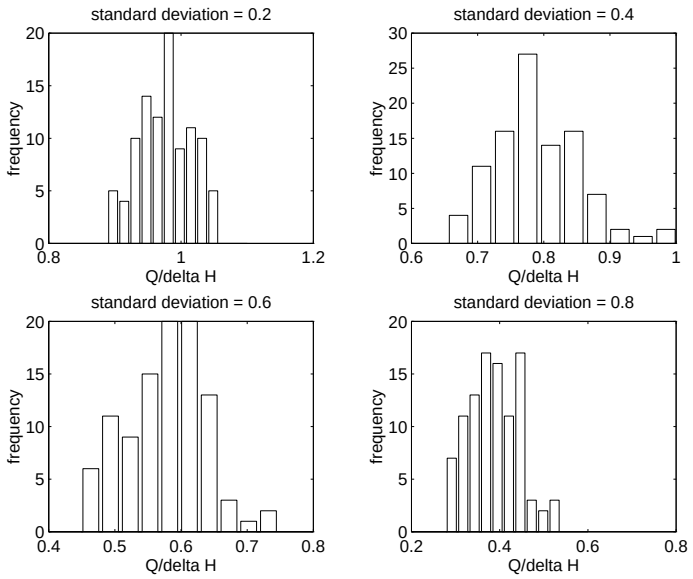

Figure 7: Variability in the ratio $Q/\Delta H$ over suites of 100 realizations of networks with randomly assigned pipe radii.

Next we examine the model's results for macroscopic, biofilm-free transport. Figure 9 shows concentration fronts entering an initially solute-free network, computed using a two-dimensional, rectangular network. Here, the macroscopic flow direction is from left to right. For $t \geq 0$, all of the fluid entering the grid has unit concentration. The top two plots show concentration fronts at time $t = 300$. The bottom two plots show mean concentration as a function of depth. The plots on the left show results for a single realization, while the plots on the right show mean concentrations computed from 50 realizations of the network, each having a different assignment of pipe radii using a lognormal distribution, with $\mu = 1$ and $\sigma = 0.6$ As the figure shows, solute distributions in a single realization typically exhibit fingering, reflecting the fact that solute advects preferentially through the larger pipes. Averaging several realizations smooths out the fingers, yielding fronts that exhibit the diffusion-like spreading associated with stochastic solute transport.

In addition to concentration fronts, we examine the transport of concentration plumes by

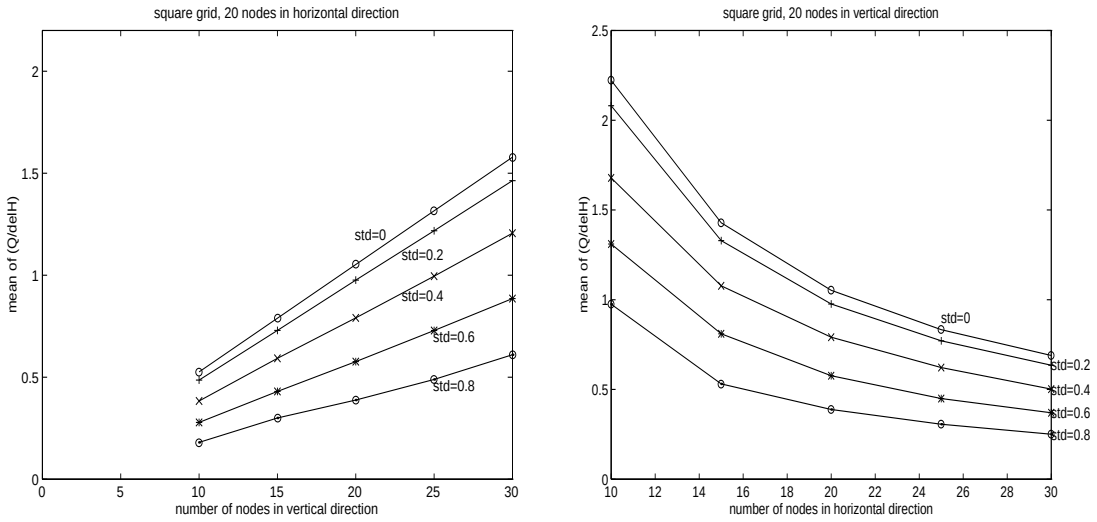

Figure 8: Dependence of flow to head drop ratio on width and length of a grid. All values plotted represent the mean of 100 realizations. The mean pore size is 1 in all realizations. Standard deviations of the log-normal distributions are shown by the curves.

assigning nonzero initial concentration in some pipes while leaving other pipes solute-free. Figure 10 shows the pipes in a 30×20 rectangular network that have unit initial concentration. All other pipes in the network have initial concentration 0. We display average values from 50 different realizations, created using a lognormal probability distribution for the pipe radii. The mean value of the radii is $\mu = 1$, and their standard deviations are $\sigma = 0.2$ and $\sigma = 0.6$.

Figure 11 shows average concentration plumes at three different times for the case $\sigma = 0.2$. The figure displays the plumes in four different ways. In the upper left is a gray-scale plot, with the shade black corresponding to concentration 0 and lighter shades corresponding to higher concentrations. The plots in the upper right are wire-mesh plots, in which height corresponds to concentration. The wire-mesh plots in the lower left and right are similar, except that they show the concentration graph from different viewing angles. The horizontal axis on the plots in the lower left corresponds to the horizontal position on the grid. These plots make it easier to see the amount of longitudinal dispersion. The horizontal axis on the plots in the lower right corresponds to the vertical position on the grid, so we can easily see the dispersion in the transverse direction.

Figure 12 shows average concentrations at $t = 300$, computed using a standard deviation $\sigma = 0.6$. The plot illustrates four trends. First, the solute plume tends to move further downstream for smaller values of σ. This trend may be attributable to the geometry of the network. At smaller values of σ, there is less tendency for fluid to bypass longitudinal pipes having unusually small radii, so there is less flow through transverse pipes and correspondingly more flow through longitudinal pipes. Second, the average concentration plumes appear rougher at larger values of σ, suggesting that more realizations need to be averaged to produce smooth profiles. Third, there is a greater transverse dispersion as σ increases, again because there is a greater tendency to bypass longitudinal pipes with small radii. Finally, larger values of σ tend to yield average plumes having greater transverse asymmetry.

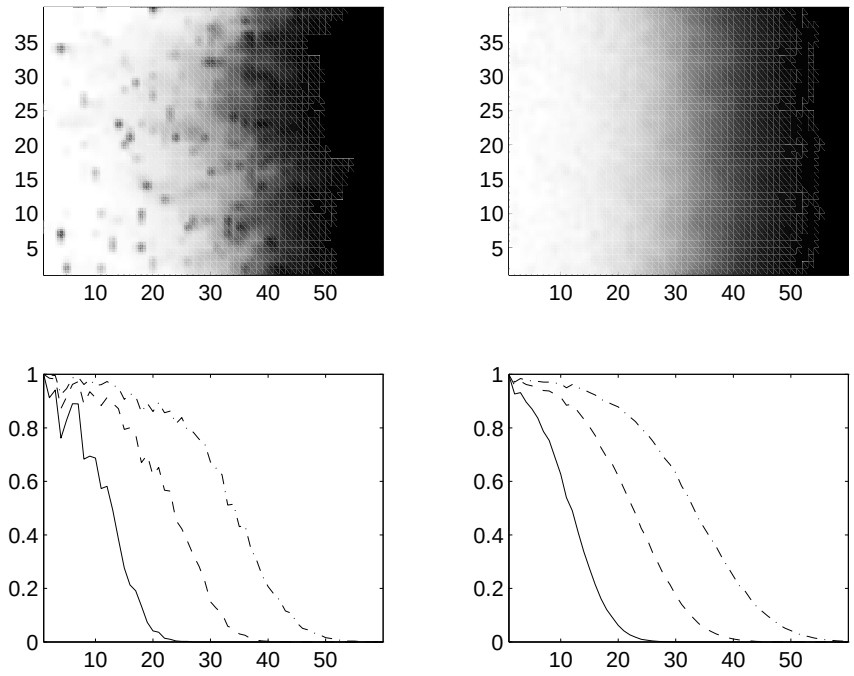

Figure 9: Concentration profiles computed on a 60×40 rectangular network. The plot on the left shows results from a single simulation. The plots on the right show mean concentrations from 50 realizations. The plots show concentration profiles at final times $t = 100$, $t = 200$, $t = 300$.

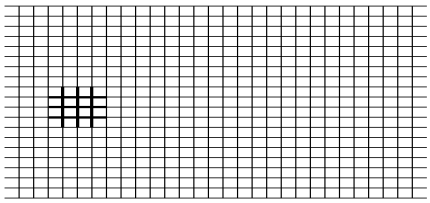

Figure 10: Initial conditions for plume transport simulations. The boldface pipes initially have unit concentration. All other pipes have initial concentration 0.

The transport results presented are similar to solutions of the advection-diffusion equation (ADE) in two and three dimensions. Macroscopic advection moves the bulk of the fluid downstream. Macroscopic diffusion occurs as the plume spreads out with time. There is one noticeable numerical artifact in figures 11 and 12. A small area in the grid, where the initial concentration is nonzero, maintains a local maximum concentration. This is not observed in solutions of the ADE. It would be interesting to see if there are physical phenomena that exhibit this type of behavior. The concentration remains high in this area because transverse pipes there have low flow velocities. Different grid arrangements might reduce this effect.

Finally, we examine whether the network models gives physically plausible results for biofilm growth and transport. A more thorough investigation of this issue along with scale-up results, may be found in a subsequent paper (Suchomel et al.). The simulations presented here mimic physical experiments like those done in soil or sand columns. Initially, all of the pipes in a 30×20,

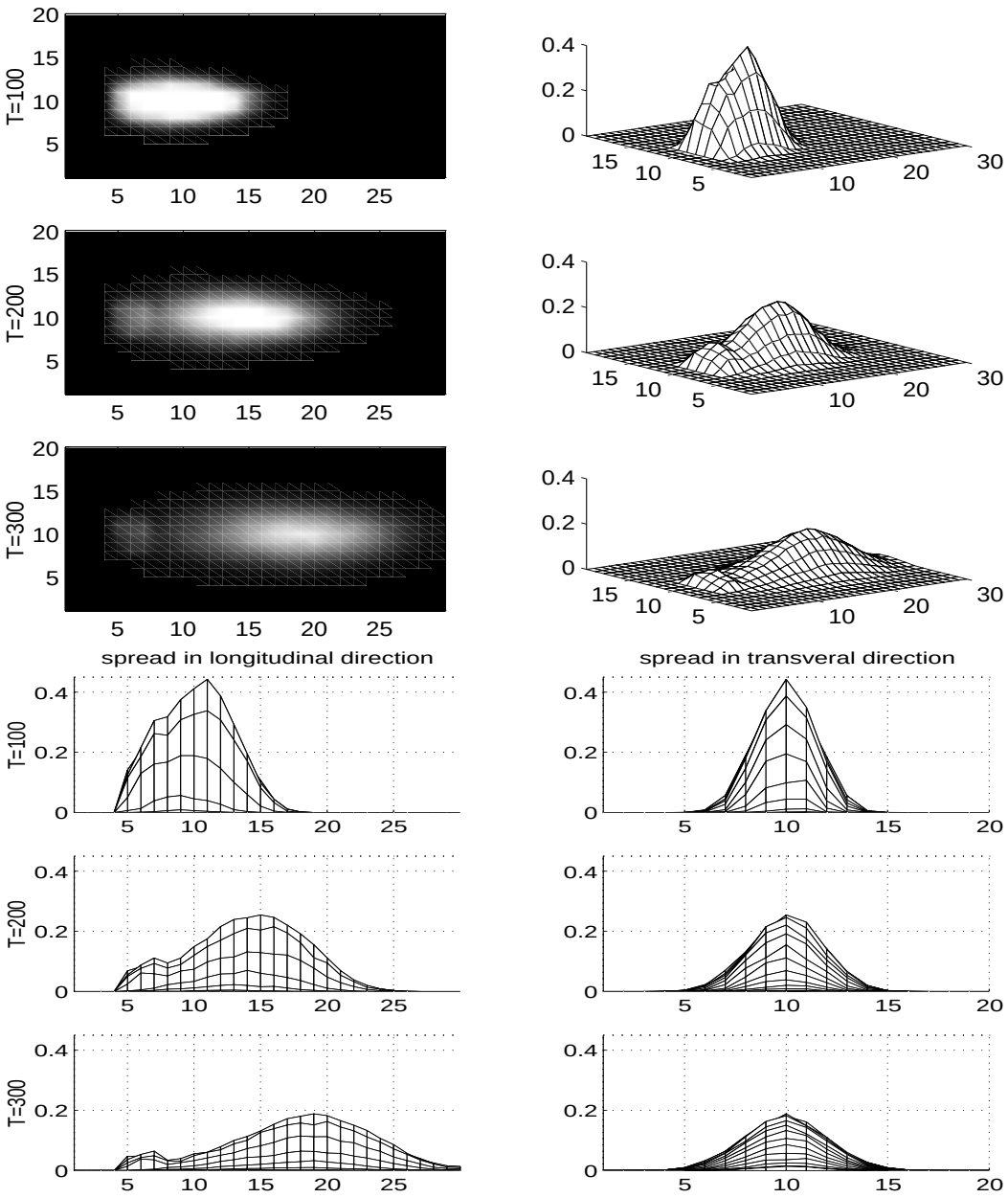

Figure 11: Ensemble-average concentrations at $t = 100$, $t = 200$, and $t = 300$ for a 30×20 network with an initial solute plume near the left edge of the network. For this ensemble, $\sigma = 0.2$.

two-dimensional network have a nutrient concentration $c_n = 0$ and a uniform adsorbed bacteria concentration $BA = 0.01$. For time $t \geq 0$, the concentration of nutrients in the fluid flowing into the network is $c_n = 1$.

Figure 13 shows results for an unstructured model that consists of only two species: nutrients and bacteria. All of the nutrients are in solution and all bacteria is in the adsorbed phase. The growth of bacteria is given by Monod reaction kinetics (Alexander, 1994). The plots show averaged

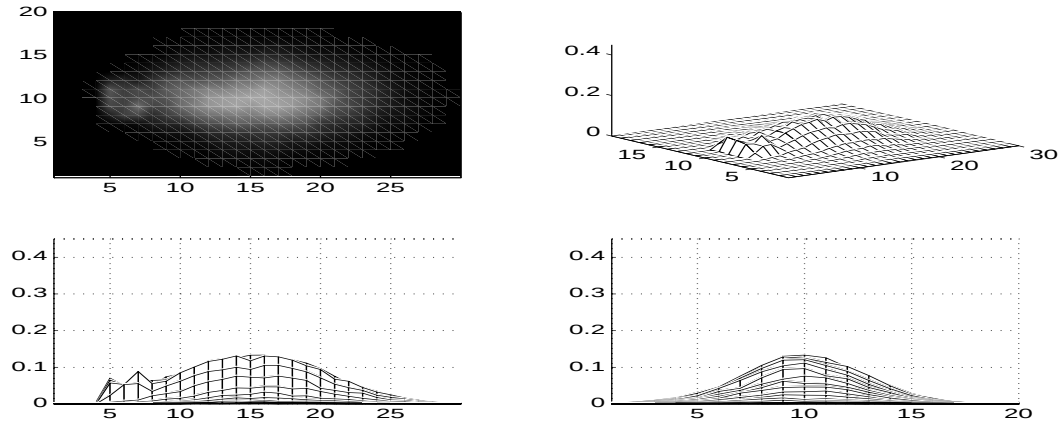

Figure 12: Average concentrations at $t = 300$ for a 30×20 rectangular network with an initial solute plume near the left edge of the network. In these plots, $\sigma = 0.6$.

values from 50 individual simulations. The concentration of bacteria steadily increases with time at the inlet side of the grid, where nutrients are entering. Corresponding decreases in normalized porosity and permeability occur as bacteria clog the pore spaces. The nutrient concentrations are shown in the upper right plot. At first the nutrients penetrate the grid and move downstream via advection and dispersion, with little being lost to reaction. As time progresses, the bacteria concentration increases near the inlet side of the grid, and the bacteria begin consuming the nutrients more rapidly. The nutrient concentration therefore gets depleted as it moves across the inlet side of the grid. At t=500, the nutrient concentration is higher at some downstream locations than it is near the inlet side. This shows that some of the nutrients find their way downstream without being consumed by the bacteria.

8 Conclusions

Network models of porous media have been in use for over 40 years. In this paper we create a new type of network simulator specifically for modeling biofilm growth and transport. In this pipe-and-junction model, the equations for the fluid flow yield a coefficient matrix that is symmetric and positive definite, and hence the system may be solved using an iterative SOR technique. We develop a new method for modeling transport in the network. This method employs an upwind, explicit finite-difference scheme within each pipe, together with a partitioning technique that enables us to bound the numerical diffusion generated in each pipe. A simple adsorption model accounts for bacteria and nutrients and their interactions. We compute macroscopic properties of the flow such as porosity and permeability and their dependence on the amount of biomass. Such a model is useful in the scale-up of microscopic dynamics to macroscopic descriptions needed in continuum-level models of biofilms in porous media. A sequel (Suchomel et al.) to this paper describes this application.

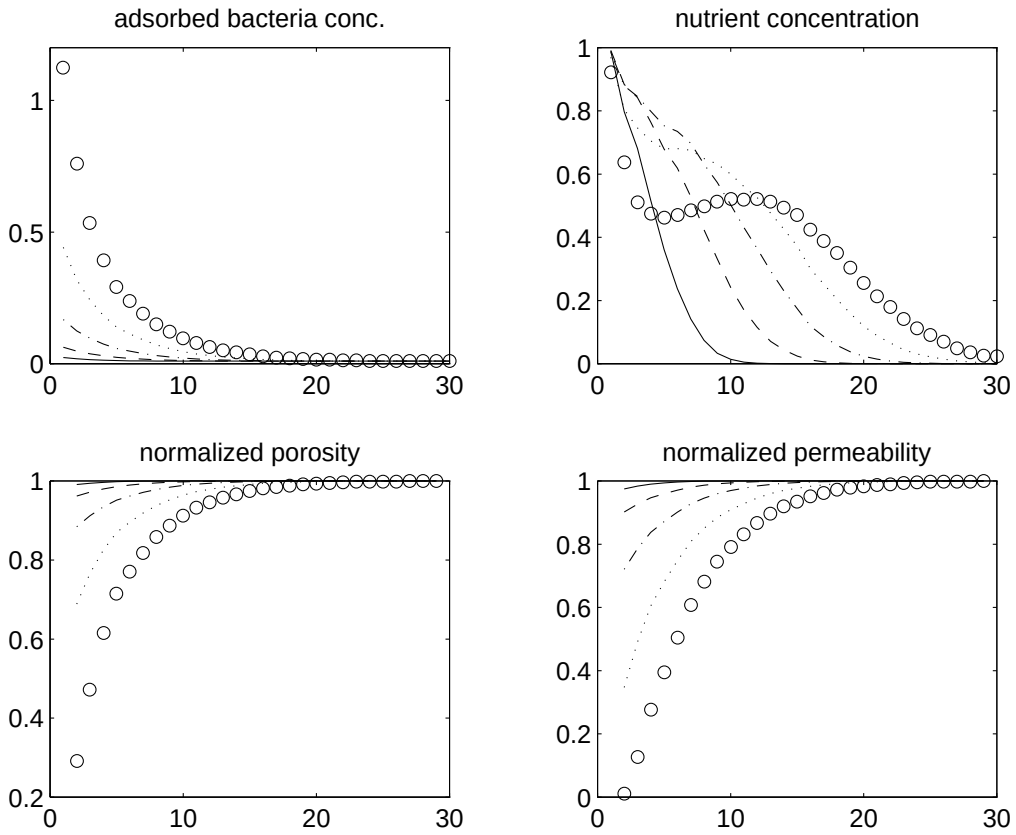

Figure 13: Average values of 100 simulations using an unstructured model. The horizontal axis is depth in a 30 by 20 grid. Pipe radii have $\mu = 1$ and $\sigma = 0.6$. Times are: — $t = 100$; – – – $t = 200$; –.–.– $t = 300$; $\cdots$ $t = 400$; ooo $t = 500$.

9 References

1. Alexander, M., 1994, Biodegradation and Bioremediation, Academic Press.

2. Brualdi, B. A. and Ryser, H. J., 1991, Combinatorial Matrix Theory, Cambridge University Press.

   question - Brian

3. Christensen, B. E. and Characklis, W. G., 1990, Physical and Chemical Properties of Biofilms, in W. G. Characklis and K. C. Marshall (eds.) Biofilms, Wiley-Interscience, New York, pp. 93-130.

4. Hull, L. C. and Koslow, K. N., 1986, Streamline Routing Through Fracture Junctions, *Water Resources Research*, **22**,(12), 1731-1734.

5. Imdakm, A. O. and Sahimi, M., 1991, Computer Simulation of Particle Transport Processes in Flow through Porous Media, *Chemical Engineering Science*, **46**, (8), 1977-1993.

6. Jerauld, G. R., Hatfield, J. C., Scriven, L. E., and Davis, H. T., 1984a, Percolation and Conduction on Voronoi and Triangular Networks: A Case Study in Topological Disorder, *J. Phys. C: Solid State Phys.*, **17**, 1519-1529.

7. Jerauld, G. R., Scriven, L. E., and Davis, H. T., 1984b, Percolation and Conduction on the 3D Voronoi and Regular Networks: A Second Case Study in Topological Disorder, *J. Phys. C: Solid State Phys.*, **17**, 3429-3439.

8. Kincaid, D. and Cheney, W.,1991, Numerical Analysis, Brooks/Cole Publishing Co., Pacific Grove, Ca., 690 pages.

9. Koplik, J., 1982, Creeping Flow in Two-Dimensional Networks, *J. Fluid Mech.*, **119**, 219-247.

10. Koplik, J. and Lasseter, T., 1982, Two-Phase Flow in Random Network Models of Porous Media, *Paper presented at* 57^{th} *Annual Fall Technical Conference and Exhibition of the Society of Petroleum Engineers of AIME.*

11. Lindqvist, R., Cho, J. S., and Enfield, C. G., 1994, A Kinetic Model for Cell Density Dependent Bacterial Transport in Porous Media, *Water Resources Research*, **30**(12), 3291-3299.

12. Philip, J. R., 1988, The Fluid Mechanics of Fracture and Other Junctions, *Water Resources Research*, **24**,(2), 239-246.

13. Rege, S. and Fogler, H., 1987, Network Model for Straining Dominated Particle Entrapment in Porous Media, Chemical Engineering Science, **42**,(7), 1553-1564.

14. Scheidegger, A. E., 1957, The Physics of Flow Through Porous Media, University of Toronto Press.

15. Simon, R., and Kelsey, F. J., 1971, The Use of Capillary Tube Networks in Reservoir Performance Studies: I. Equal-Viscosity Miscible Displacements, *Society of Petroleum Engineers Journal*, **11**, 99-112.

16. Simon, R., and Kelsey, F. J., 1971, The Use of Capillary Tube Networks in Reservoir Performance Studies: II. Effect of Heterogeneity and Mobility on Miscible Displacement Efficiency, *Society of Petroleum Engineers Journal*, **12**, 345-351.

17. Suchomel, B. J., Chen, B. M. and Allen, M. B., Macro-scale Properties in Porous Media from a Network Model, *submitted.*

18. Sugita, F., Gillham, R. W., and Mase, C., 1995, Pore Scale Variation in Retardation Factor as a Cause of Nonideal Breakthrough Curves: 2. Pore Network Analysis, *Water Resources Research*, **31**,(1), 113-119.

19. Tan, Y., Gannon, J. T., Baveye, R., and Alexander, M., 1994, Transport of Bacteria in an Aquifer Sand: Experiments and Model Simulations, *Water Resources Research*, **30**,(12), 3243-3252.

20. Taylor, S. W., and Jaffé, P. R., 1990a, Biofilm Growth and the Related Changes in the Physical Properties of a Porous Medium 1. Experimental Investigation, *Water Resources Research*, **26**,(9), 2153-2159.

21. Taylor, S. W., Milly, P. C. D., and Jaffé, P. R., 1990b, Biofilm Growth and the Related Changes in the Physical Properties of a Porous Medium 2. Permeability, *Water Resources Research*, **26**,(9), 2161-2169.

22. Taylor, S. W. and Jaffé, P. R., 1990c, Biofilm Growth and the Related Changes in the Physical Properties of a Porous Medium 2. Dispersivity and Model Verification, *Water Resources Research*, **26**,(9), 2161-2169.

23. van Brakel, J., 1975, Pore Space Models for Transport Phenomena in Porous Media, Review and Evaluation with Special Emphasis on Capillary Liquid Transport, *Powder Technology*, **11**, 205-236.

24. Vandevivere, P., and Baveye, P., 1992, Effect of Bacterial Extracellular Polymers on the Saturated Hydraulic Conductivity of Sand Columns, *Applied and Environmental Microbiology*, **58**, (5), 1690-1698.

25. Young, D. M., 1971, Iterative Solution of Large Linear Systems, 1971, Academic Press, New York, 570 pages.